Vol. 15 • No. 50 • December 13 • 2019

www.small-journal.com

NANO · MICRO small

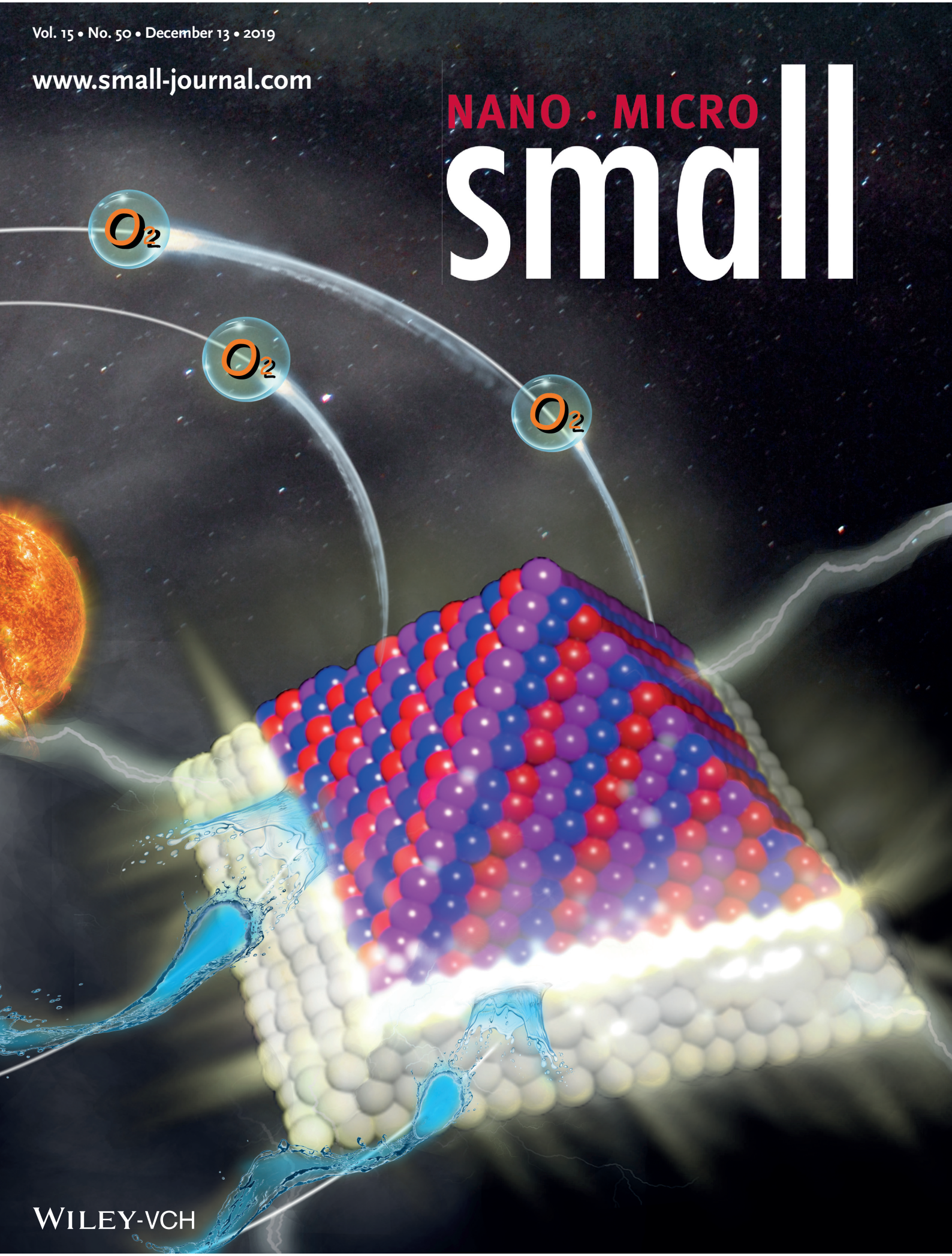

WILEY-VCH

NANO · MICRO small
www.small-journal.com

Discontinuity-Enhanced Thin Film Electrocatalytic Oxygen Evolution

Ming-Chi Shih, Ren-Huai Jhang, Ya-Ting Tsai, Chia-Wei Huang, Yung-Jr Hung, Mei-Yi Liao, Jiaxing Huang, and Chun-Hu Chen**

Thin film electrocatalysts allow strong binding and intimate electrical contact with electrodes, rapid mass transfer during reaction, and are generally more durable than powder electrocatalysts, which is particularly beneficial for gas evolution reactions. In this work, using cobalt manganese oxyhydroxide, an oxygen evolution reaction (OER) electrocatalyst that can be grown directly on various electrodes as a model system, it is demonstrated that breaking a continuous film into discontinuous patches can significantly enhance the overall OER performance without sacrificing long-term stability even under elevated electrocatalytic stress. Discontinuous films with higher edge-to-area ratios exhibits reduced overpotentials, increased turnover frequency, and more pronounced current increase after electrochemical conditioning. Operando Raman spectroscopy studies during electrocatalysis reveal that the film edges require lower potential barrier for activation. Introducing discontinuity into thin film electrocatalysis can thus lead to the realization of high performance yet highly robust systems for harsh gas evolution reactions.

1. Introduction

The increasing demand of clean energy drives the emerging of water splitting to support self-sustainable energy storage of green powers (e.g., solar, wind, etc.) and hydrogen fuel generation.[1–7] To support the future commercialization of water splitting, low-cost and facile fabrication of electrocatalysts, active for oxygen evolution reaction (OER) without involving precious metals (e.g., Ru and Ir), is therefore the central interests.[8,9] General approaches and knowledge capable of enhancing atom-efficiency in OER are also essential to conserve all the elements used in electrocatalysts regardless the individual nature abundance.

As compared to colloidal electrocatalysts, scalable thin film electrocatalysts have been recognized by rapid mass transfer and robust adhesion with electrodes against peeling of electrocatalytic materials during oxygen bubbling, essential to achieve durable water splitting, high power output, and commercial demand of coating on various substrates.[10] The previous OER studies have concentrated on exploring continuous, void-free thin films of Ni, Co, Fe, and Mn oxides in alkaline conditions,[5,10–19] revealing the important electrocatalytic influence regarding crystal structures, synergistic behaviors between elements, catalytic roles of active species, alternation of orbitals and electron transfer, and deposition methodologies. As electrocatalytic OER requires electricity (anodic current) and mass transport of reactants (water/OH^-) and product (O_2) at catalytic sites to proceed, this so-called "triple-phase boundary region,"[20] usually at the heterojunction edges, is anticipated to deliver the best OER activities. By dividing a continuous thin film into fractured, discontinuous pieces (as a concept of "thin film imperfection"), the additionally exposed edge sites can thus greatly improve OER performance and atom efficiency. Recent designs of single atom catalysts may further support this idea.[21,22] In fact, strong edge effects on improving hydrogen evolution reaction (the other half reaction in water splitting) have been well recognized.[23,24] However, this concept of edge exposure in thin film has received much less attentions possibly due to the investigation complexity and coverage uncertainty of discontinuous deposition. With the example of photolithography-patterned electrocatalysts toward improved OER,[25] correlation of OER performance to systematic edge exposure normalizing to unit area is then becoming the most desired information. Recent study on the edge-site atom population of discrete, atom-scale deposition of iron oxides shows a proportional relationship to OER activities.[26] Despite the emerging of edge-dependent OER, reliable deposition over large area with versatile coverage/continuity to achieve

M.-C. Shih, R.-H. Jhang, Y.-T. Tsai, Prof. C.-H. Chen
Department of Chemistry
National Sun Yat-sen University
Kaohsiung 80424, Taiwan
E-mail: chunhu.chen@mail.nsysu.edu.tw
R.-H. Jhang, Prof. J. Huang
Department of Materials Science and Engineering
Northwestern University
Evanston, IL 60208, USA
E-mail: jiaxing-huang@northwestern.edu
C.-W. Huang, Prof. Y.-J. Hung
Department of Photonics
National Sun Yat-sen University
Kaohsiung 80424, Taiwan
Prof. M.-Y. Liao
Department of Applied Chemistry
National Pingtung University
Pingtung 90004, Taiwan
The ORCID identification number(s) for the author(s) of this article can be found under https://doi.org/10.1002/smll.201903363.

DOI: 10.1002/smll.201903363

a wide-scale edge exposure poses another difficulty in sample preparation. Furthermore, the individual mass of discontinued coating is significantly insufficient to properly monitor in situ microstructural evolution directly under water. The durability, unusual behaviors, and magnitude of OER enhancement due to thin film imperfection still remain elusive.

In our previous work, the redox-assisted deposition of cobalt manganese oxyhydroxide (CMOH, $Co_9Mn_3O_{26}H_{13}$) characteristic with extraordinary OER activities, ability of mask patterning, high coating uniformity, and strong adhesion is therefore ideal for realizing model samples of discontinuous films for OER study.[1,27] Raman spectroscopy is exclusively useful to address the challenge of acquiring molecular changes of active sites without water interference, but also disadvantageous in weak signals.[28,29] Hence we introduced surface-enhanced Raman scattering with gold surface to generate sufficient signals for microscopic evolution of the thin films while performing OER in water.[30]

Herein, we directly revealed that the greatly improved OER performance by systematically increasing thin film discontinuity, where the magnitude of electrocatalytic improvement was proportional to edge-to-area ratios of films. By maximizing the ratios through mask-assisted deposition of CMOH on gold-coated pyramidal electrodes, only 1.8% mass of the fully covered deposition was required to achieve the same OER current with and exhibited a 56-time higher turnover frequency (TOF) than continuous thin film samples. Unusually, despite the high current flux and catalytic stress due to the elevated TOF, the most discontinuous samples exhibited exceptional stability for 720 h of water splitting with negligible decay. The heterojunction edges of the coatings are found activated prior to the central parts of CMOH deposition, responsible for the enhanced atom-efficiency and performance proportional to the degrees of thin film discontinuity.

2. Results and Discussion

2.1. Model Study of Effect of Discontinuity on Thin Film OER Catalyst

In assessing the edge effect of thin film imperfection on OER, a series of model samples were fabricated with well-defined patterns of CMOH thin film on flat substrates of both fluorine-doped tin oxide (FTO) and Au-coated Si substrates, accomplished by placing these substrates in an acidic aqueous environment (pH = 4.26) containing $KMnO_4$ and $Co(OAc)_2$ at 80 °C. The highly oxidative $KMnO_4$ drives the redox reaction with Co(II) to enable strong adhesion and intimate contact with diverse substrates to yield uniform coatings without thermal annealing.[1] The acidic environments indicate a redox growth pathway of CMOH with homogeneous element distribution different from the precipitation method commonly starting with divalent manganese and cobalt ions with inconsistent K_{sp} conditions.[31] The continuous CMOH (1×1 cm^2) electrodes and discontinuous ones (25 isolated pieces with a total coverage area of 1 cm^2 identical to the coverage of continuous ones) were tested for electrocatalytic OER comparison (**Figure 1**a,b). The linear sweep voltammetry (LSV) results show a similar trend that the discontinuous CMOH on both the substrates exhibits greater OER performance as the overpotentials lowered than the continuous ones (Figure 1a,b), indicating that the edge enhancement may generally occur independent on specific substrate materials, although some specific case on gold has been reported.[26,32] In addition, the varied distance between each isolated CMOH pieces on the both substrates shows no appreciable influence on the LSV results (Figure S1, Supporting Information). The interdistance between each isolated coating was not concerned in the electrocatalyst patterning for the later investigation of this work.

A horizontal setup of the electrodes allows the direct observation of the oxygen-evolution sites. As shown in Movie S1 in the Supporting Information, the locations of oxygen generation were observed mainly around the interface between CMOH and the gold surface (Figure 1e), rather than the center area of coating, both in the continuous and discontinuous cases. By applying much higher potentials, it was found that oxygen bubbles came from the whole deposition (both isolated and continuous ones) with no obvious preference of the edges or central spots. These results indicate that the heterojunction edges require a lowered activation potential than the other parts of the deposition.

To further verify this concept, we used resin paints to cover the edges of both continuous and discontinuous CMOH deposition yet giving the identical total exposure area of the central parts for electrochemical comparison (Figure 1c,d). After the edges shielded by nonconducting polymer, the same OER current density (e.g., 10 mA cm^{-2}) would need additional potentials to reach, compared to the nonshielding samples. This behavior was both observed in the continuous and discontinuous thin film samples. These results verify the higher potential barriers of the center parts that require higher potentials to initiate OER. In addition, the edge sites act as the ideal triple-phase boundary region due to the characteristics of low-potential activation and efficient mass transport of electrolyte accessibility and oxygen elimination. The discontinuity-dependent OER behaviors are therefore representing a promising approach to modulate the water splitting performance through edge creation. As the magnitude of OER enhancement by thin film imperfection has not been studied yet, the following work concentrated on the impacts of fine-scale thin film imperfection and the mechanistic insights through in situ studies.

2.2. Edge Enhanced CMOH Films on 3D Substrate

To achieve a series of edge exposure in a controllable manner at finer scales, we conducted a facile photoresist-mask deposition of CMOH on pyramid-textured substrates. Micron-scale pyramidal features on Si wafer, widely used in solar cell industry as antireflective layers, can be easily adopted and scaled up by anisotropic alkaline etching on commercial Si (100) wafers.[33] In addition, 3D features facilitate oxygen elimination, which is desired to decouple its correlation with overall performance for a fair comparison of turnover frequency.[10,34] The preparation of discontinuous CMOH thin film on top of individual Au/Si pyramids was illustrated as **Scheme 1** (see the detailed procedure in the Supporting Information). After

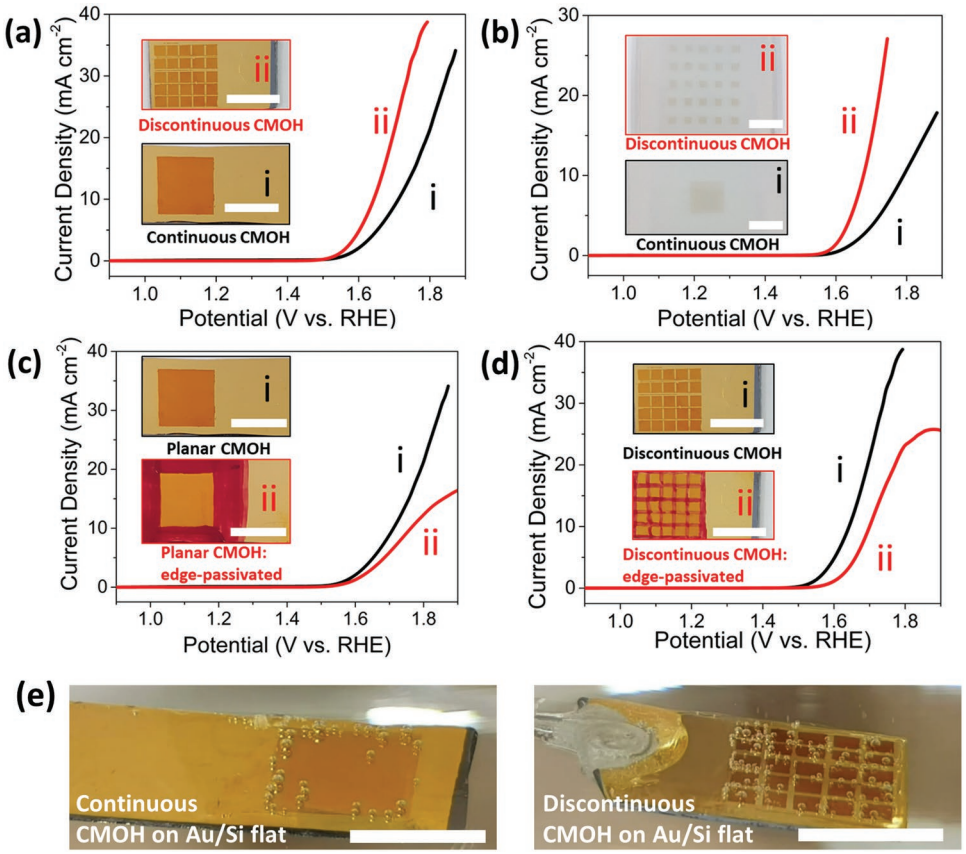

Figure 1. Electrocatalytic OER current density of continuous and discontinuous CMOH thin films grown on planar a) gold/Si wafers and b) FTO. Discontinuous films perform better despite of having the same area as the continuous ones. In (c) and (d), it compares catalytic performances before and after edge passivation. The edges of both c) continuous and d) discontinuous films are passivated by an inactive red coating based nail polish. The current-saturated curves after 1.8 V were due to the limitations toward mass transport of oxygen evolution by impairing edge-passivation. e) Snapshots of Movie S1 in the Supporting Information show that the film edges are the preferential site for oxygen evolution for both the continuous and discontinuous films. All the scale bars are 1 cm.

the fabrication of pyramidal textures on Si wafers, a thin layer of gold was deposited over the entire surface of the substrates. Subsequently, a spin-coated layer of photoresist covers the Au/Si pyramidal substrates (1 × 1 cm^2). By increasing the oxygen-plasma etching time for photoresist removal (i.e., 1, 2, 3, and 4 min), a greater area of the pyramidal tips can be exposed. Thin film CMOH was then deposited on the entire surface of photoresist following the identical procedure used to fabricate the CMOH electrodes in Figure 1. After the removal of photoresist by acetone, these samples yielded the different degrees of CMOH coverage on the pyramid tip, denoted as small (CMOH-py-S), medium (CMOH-py-M), large (CMOH-py-L), and extra-large coverage (CMOH-py-XL) under the etching time of 1, 2, 3, and 4 min, respectively. The control samples of continuous CMOH (full coverage of 1 × 1 cm^2) on pyramids substrates are named as CMOH-py-cont.

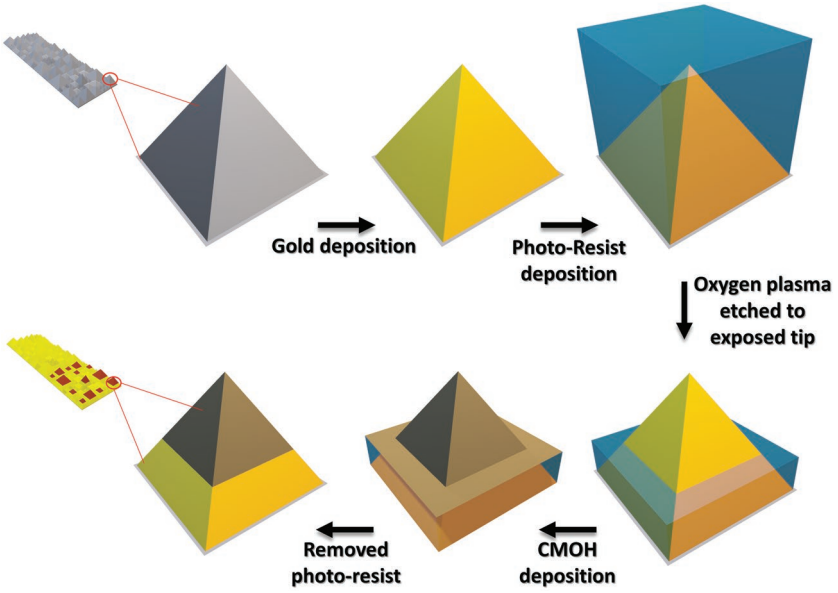

Scheme 1. Schematic drawings illustrating the fabrication procedure of CMOH thin coating over arrays of gold plated Si pyramidal electrodes. Note the dimension variation among each Si pyramids.

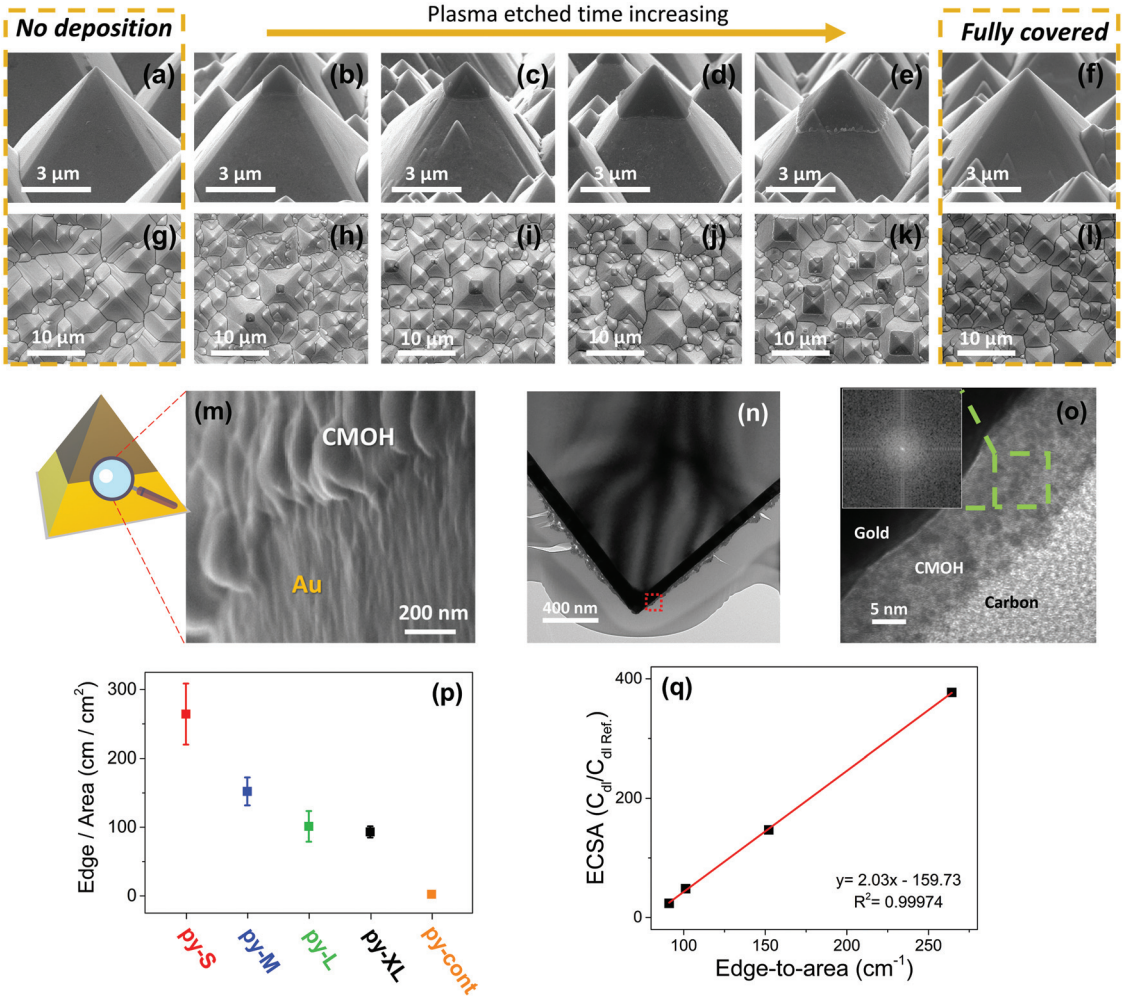

Figure 2. CMOH grown on gold-plated Si pyramids. SEM images showing the a–f) side and g–l) top views of Au/Si pyramids with increasing loading of CMOH to eventually achieve a complete coverage: a,g) bare Au/Si substrate, b,h) CMOH-py-S, c,i) CMOH-py-M, d,j) CMOH-py-L, e,k) CMOH-py-XL, and f,l) complete coverage of CMOH. m) High magnification SEM image showing the morphology of the edge of a CMOH film grown. n,o) Cross-sectional HR-TEM images showing the interface between CMOH coating and the underlying Au/Si layer on a sample prepared by FIB. The area shown in (o) corresponds to the red square in (n). The inset of (o) shows the FFT pattern corresponding to the area marked by the green square, indicating amorphous nature of the grown CMOH. p) Edge-to-area ratio of CMOH coating decreases as the coverage increases based on measurements on SEM images. q) Plotting electrochemical surface area against edge-to-area ratio reveals a linear correlation.

The scanning electron microscope (SEM) images show the CMOH coatings (the dark contrast parts) on the tips of individual pyramids (**Figure 2**). Among these samples, CMOH-py-S shows the smallest coverage both on the tips and the entire substrates (see both the top- and side-view images). The increased CMOH coverage and continuity were observed along with the extended plasma etching time. The control samples with completely continuous CMOH deposition were also prepared for electrocatalytic OER comparison (Figure 2f,l). The film coverage was statically estimated to be 9.200 (±4.309) × 10^{-3}, 2.498 (±1.362) × 10^{-2}, 1.017 (±0.351) × 10^{-1}, and 2.091 (±0.368) × 10^{-1} (cm^2) in CMOH-py-S, CMOH-py-M, CMOH-py-L, and CMOH-py-XL, respectively (see the method described in the Figure S2, Supporting Information). As more fractured films should give higher quantity of exposed edges per unit coverage, the degrees of film discontinuity were indexed by the ratios of total edge length normalized by area of isolated deposition (i.e., edge/area in unit of cm^{-1}). The higher values of the edge-to-area ratios reflect the greater degrees of imperfection, and higher percentages of exposed edges of an individual coating. The discontinuity of CMOH-py-S, CMOH-py-M, CMOH-py-L, and CMOH-py-XL was estimated to be 264.27 ± 44.48, 152.16 ± 20.34, 101.22 ± 22.36, and 93.10 ± 8.18 (cm^{-1}), respectively (Figure 2p and Figure S3, Supporting Information). The electrochemical surface area (ECSA) of these discontinuous samples was measured and showed a linear relationship to the edge-to-area ratios (Figure 2q and Figure S4, Supporting Information), further verifying the efficacy of the adopted statistics consistent with the experimental measurement in estimating quantity of exposed edges. The total surface area of CMOH-py-cont was based on the geometry in Figure S2 in the Supporting Information. In addition, the as-deposited CMOH was characterized by focused ion beam (FIB) and high-resolution transmission electron microscopy (HR-TEM) (Figure 2n,o), showing the typical thickness close

to 15 nm with amorphous features revealed by the fast-Fourier-transform (FFT) patterns (Figure 2o inset), which has been proved to be highly active for OER.[1,11,35]

The usage of X-ray photoelectron spectroscopy (XPS) and inductively coupled plasma mass spectrometry (ICP-MS) can verify the oxidation states and composition of the deposited CMOH. In CMOH-py-cont samples, ICP-MS determined the observed chemical formula of the CMOH thin film to be $Co_9Mn_3O_{26}H_{13}$.[1] In the XPS results (Figure S5a, Supporting Information), the resulting Co:Mn ratio (Co/Mn = 3.0) coincides with both the ICP-MS results (Co/Mn = 2.9) and the results from the deposited CMOH on other substrates (e.g., fluorine-doped tin oxide). In terms of the metal oxidation states, the binding energy peaks in the Co 2p spectra (Figure S5b, Supporting Information) at 780.8 and 796.2 eV, corresponding to Co $2p_{3/2}$ and $2p_{1/2}$, respectively, as well as the satellite peaks at 791.0 eV indicate the presence of Co(III).[36] Meanwhile, indication of Mn (IV) is reflected on the presence of peaks at 642.2 and 654.0 eV, corresponding to Mn $2p_{3/2}$ and Mn $2p_{1/2}$, respectively (Figure S5c, Supporting Information).[27] The strong hydroxide signals at 532 eV and a weak O^{2-} signal at 530.3 eV in the O 1s spectra (Figure S5d, Supporting Information) further support the chemical formula above.

The OER performance was first evaluated by LSV in 0.1 M KOH, and summarized in **Table 1**. CMOH-py-S exhibits the smallest overpotential (η at 30 mA cm^{-2}) of 361 mV, while the others show the higher values of 406 mV (CMOH-py-M), 453 mV (CMOH-py-L), and 476 mV (CMOH-py-XL). CMOH-py-cont with the completely continuous deposition shows a large overpotential of 632 mV. In the enlarged LSV diagram (Figure S6b, Supporting Information), the redox peaks near 1.42 V can be observed in each sample, attributed to the oxidation signal of Co^{3+} to Co^{4+} transition critical to reach OER-active configurations.[35] These high valence sites were reported to facilitate adsorption of hydroxide ions and subsequent deprotonation to generate molecular oxygen. The general trend shows that the peak intensity increases as the sample discontinuity increases. The greatest intensity in CMOH-py-S suggests the highest degrees of Co^{3+}/Co^{4+} activation, which agrees with the best LSV performance in **Figure 3**a. In contrast, the absence of this transition in CMOH-py-cont indicates a relatively low activation yields in the continuous thin film.

We conducted electrochemical conditioning to further study the discontinuity-dependent activation with a constant supply of anodic current, where atomic arrangements and/or phase transformation of electrocatalysts gradually evolve into the OER-active configurations over time.[11,35,37] As shown in Figure 3b, at the beginning of the conditioning, all of the samples exhibit the increasing of current density in different magnitude, which roughly saturated at the first 5 h conditioning and reached the values of 75.02 mA cm^{-2} (CMOH-py-S), 29.03 mA cm^{-2} (CMOH-py-M), 10.70 mA cm^{-2} (CMOH-py-L), and 5.45 mA cm^{-2} (CMOH-py-XL), corresponding to the current enhancement of 1500%, 580%, 214%, and 109%, respectively, by referencing the initial current density (5 mA cm^{-2}). Such the unusually high increase of 1500% OER current density in electrochemical conditioning has not been reported in the other similar systems during the conditioning.[1,11,26] The first 5 h stage of current climbing may reflect the intrinsic capacity of Co^{3+}/Co^{4+} and phase activation; the upper limits of current density saturation may suggest that certain quantity of idle sites is not allowed to be further activated regardless of extension of the conditioning time. Activation capacity seems to be highly dependent on the thin film discontinuity. CMOH-py-S exhibits the highest activation ratios, or the lowest idle-site percentages otherwise, among all the samples. In contrast, the more continuous sample such as CMOH-py-XL shows the much less activation capacity under the same experimental conditions.

By further comparing the LSV curves after the conditioning (Figure S6, Supporting Information), the samples with higher discontinuity generally gain the greater residue of OER improvement. CMOH-py-S exhibits the greatest activation residue by reducing the overpotential from 361 to 316 mV after the electrochemical conditioning tests. In addition, all the peaks of Co^{3+}/Co^{4+} transition in these samples became negligible after the conditioning (Figure S6b, Supporting Information), particularly the strongest one observed in CMOH-py-S. This suggests the irreversible activation and enhancement residue proportional to the coating discontinuity. The maximum limits of OER activation, also considered as limits of atom efficiency, are thus verified to be dependent on the film discontinuity. In addition, the Tafel slopes summarized in Figure S7 in the Supporting Information show the values of 59.72 mV dec^{-1} (CMOH-py-S), 60.22 mV dec^{-1} (CMOH-py-M), 61.83 mV dec^{-1} (CMOH-py-L), 61.97 mV dec^{-1} (CMOH-py-XL), and 78.85 mV dec^{-1} (CMOH-py-cont). All the discontinuous samples exhibit values close to each other,[38] suggesting the similar OER kinetics.

We demonstrated the comparison of TOF as a function of overpotentials in Figure 3c.[34] The calculation for TOF considers cobalt sites in CMOH because they serve as the main active sites for electrocatalytic OER, according to various reports.[1,19,39,40] To reach a TOF value of 5 (s^{-1}), the potentials required for each samples are 1.570 V (CMOH-py-S), 1.629 V (CMOH-py-M), 1.736 V (CMOH-py-L), and 1.775 V (CMOH-py-XL), while the continuous samples (CMOH-py-cont) need potentials far beyond 2 V to achieve. At overpotential of 0.3 V, the TOF values of each samples are 1.050 s^{-1} (CMOH-py-S), 0.300 s^{-1} (CMOH-py-M), 0.100 s^{-1} (CMOH-py-L),

Table 1. The summary of electrochemical data.

Sample	Film coated area [cm^2]	η at 30 mA cm^{-2} [mV]	Tafel slope [mV dec^{-1}]	$TOF_{\eta=0.3}$ [s^{-1}]
CMOH-py-S	$9.200(\pm4.309)\times10^{-3}$	361	59.72	1.050
CMOH-py-M	$2.498(\pm1.362)\times10^{-2}$	406	60.22	0.300
CMOH-py-L	$1.017(\pm0.351)\times10^{-1}$	453	61.83	0.100
CMOH-py-XL	$2.091(\pm0.368)\times10^{-1}$	476	61.97	0.0753
CMOH-py-cont	1.732	632	78.85	0.0188

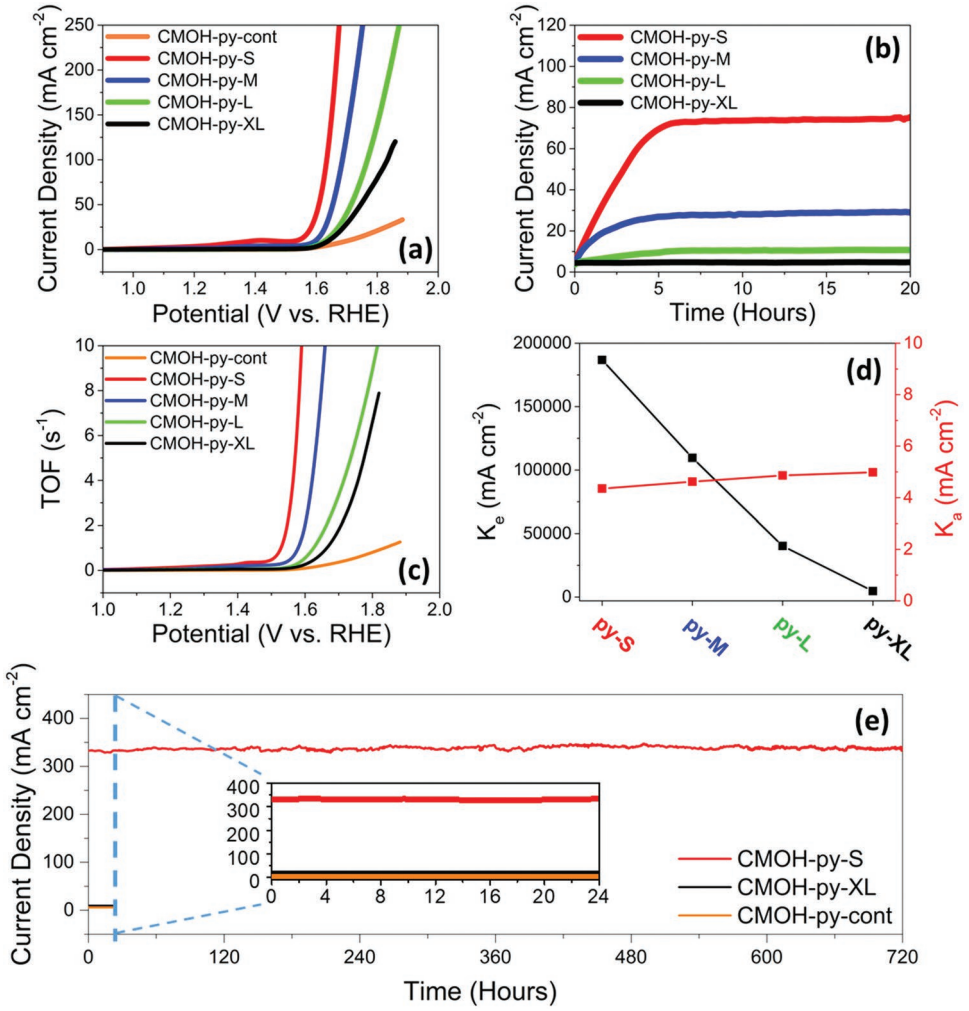

Figure 3. OER performance of CMOH films with different coverages. a) Linear-sweep voltammetry of the samples with varied CMOH discontinuity. b) Electrochemical conditioning as the function of time, c) TOF comparison after the electrochemical conditioning, d) The comparison of current contribution coefficient of K_{Edge} and K_{Area} (mA cm^{-2}) as the discontinuity (also edge-to-area ratios) of the samples. e) The OER stability tests among varied discontinuity, where CMOH-py-S with the much higher current density and electrocatalytic stress still exhibited an exceptional durability after 720 h of OER.

0.0753 s^{-1} (CMOH-py-XL), and 0.0188 s^{-1} (CMOH-py-cont), as shown in Figure S6c in the Supporting Information. The TOF of the most discontinuous sample (CMOH-py-S) is 56 times higher than the continuous ones and higher than the other reported thin film systems (Table S1, Supporting Information). Assuming that one active site yields one oxygen molecule per cycle, CMOH-py-S may possess the overall active sites 56-time higher than CMOH-py-cont per mass. Accordingly, only 1/56 mass of the fully continuous deposition is as OER-active as CMOH-py-S. The atom efficiency of CMOH-py-cont is thus as low as 1.8% compared to CMOH-py-S.

In the stability tests, CMOH-py-S, CMOH-py-XL, and CMOH-py-cont exhibit the highly stable current density of 330, 10, and 6 mA cm^{-2}, respectively, for 24 h (Figure 3e). Electrocatalysts generally suffer from a more rapid deactivation under elevated TOF. CMOH-py-S with a much higher TOF can still conduct high-performance OER without compromising the durability. The intrinsic amorphous feature of CMOH may benefit the long-term stability by providing flexibly microstructural alternation of dynamic molecular bond dissociation/formation during OER catalytic cycles.[1,28,35,41] In order to inspect any decay that may occur after an even longer operation, the durability tests were further extended to a total of 720 h on a basis of daily 20 h operation (Figure 3e). With the absence of current density decay, the concept of thin film imperfection has been successfully addressing several challenges of low atom consumption, scalable production, high activity, and reliability for the future commercialization.

We conducted operando Raman-coupled electrocatalysis (see Supporting Information for the instrumental setup) to investigate the influence of discontinuity on microstructural activation and OER performance (**Figure 4**). At 0.865 V, CMOH-py-XL exhibits intense Raman bands at 503 and 620 cm^{-1}, with a slight blueshift from amorphous trivalent cobalt oxides (e.g., 465 and 593 cm^{-1}), due to the presence of structure substitution of manganese oxide (≈25% atomic percent) (Figure 4b).[1,28,42,43] In contrast, no appreciable signals can be observed in CMOH-py-S due to the much smaller mass of the deposition (Figure 4a).

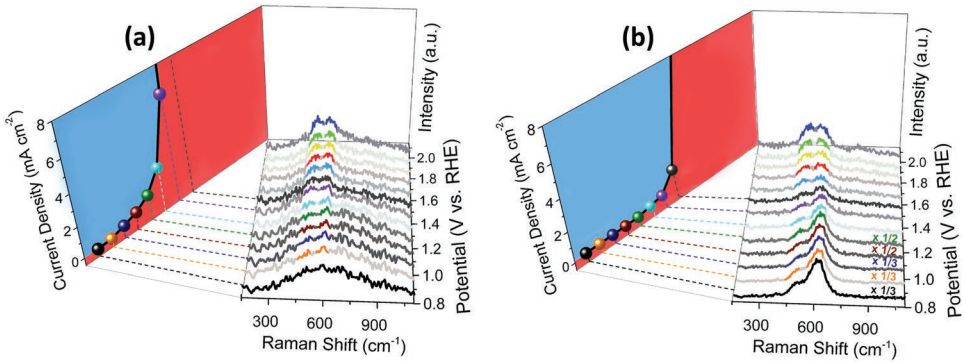

Figure 4. Operando Raman study showing the evolution of the samples a) CMOH-py-S and b) CMOH-py-XL as the applied potential is increased from 0.865 to 2.065 V with an interval of 0.1 V during OER.

At 2.065 V, where CMOH is fully activated for OER (current density >> 10 mA cm^{-2}), both the samples show the bands at 496 and 572 cm^{-1} with the similar intensity, corresponding to E_g and A_{1g} modes of layered hexagonal CoO_2[28] and consistent with the observed Co^{3+}/Co^{4+} activation in Figure 3.

Starting from 0.865 to 2.065 V, both the Raman signal and current density gradually increased in CMOH-py-S. Between 1.065 and 1.465 V, the onset of OER was coupled with the band emerging at 490 and 599 cm^{-1} with intensity of 1:1.5 (baseline corrected). At 1.565 V, E_g and A_{1g} of activated CoO_2 species are present with the intensity ratios close to 1, similar to that observed at 2.065 V; by increasing potentials from 1.565 to 2.065 V, the band intensity becomes stronger without shift in wavenumber. The stage of 1.065–1.465 V is therefore most likely corresponding to the activation process. On the other hand, for CMOH-py-XL, the typical characteristics were the decreasing of band intensity from 0.865 to 1.465 V with no onset of OER currents (Figure 4b). By referencing with CMOH-py-S, these results suggest the higher energy barrier for the more continuous deposition to initiate OER, as the onset potential delay by 500 mV was observed. The sudden current shooting at 1.565 V in CMOH-py-XL may further support the existence of high potential threshold toward activation.

The spectroscopic evolution of these two samples approaching the final activated form is completely opposite, particularly the band intensity. A more detailed study may be needed to understand whether any difference may exist in their activation pathways.[37,41] In terms of their common similarity, after the appearance of the activated form, the only change is peak intensity proportional to the applied potentials without any form of peak shift or alternation. The Raman spectrum of activated CMOH might therefore be attributed to the simultaneous monitoring of dynamically exchanged intermediates in OER electrocatalytic cycles,[28] rather than the vibration signal of a single species. The higher applied potentials overcome the resistance barrier to increase the quantity of these electrocatalytic involved species. This operando spectroscopic information could be valuable to directly distinguish active/idle states and future mechanism study into OER insight.

Increased edge-to-area ratios via thin film imperfection have been proven to achieve higher atom efficiency, easier activation, and overall the superior OER performance, but the true enhancement governed by whether the relative ratios between edge and area or the actual activity improvement occurred at edge is still not clear. To estimate the contributing portions between edge and area (also conceptually referred to as nonedge parts) to the overall OER currents, we solved the *K* factors in the following equation[44]

$$K_{\text{Edge}}S_{\text{Edge}} + K_{\text{Area}}S_{\text{Area}} = \text{Overall current} \quad (1)$$

where K_{Edge} and K_{Area} are the current contributing coefficients (mA cm^{-2}) of edge and area, respectively; S_{Edge} and S_{Area} are the surface area of edge and area (cm^2), respectively. S_{Edge} is estimated as the product of edge length multiplied by the CMOH film thickness of 15 nm observed in Figure 2o. By plugging in the values of S_{Edge}, S_{Area}, and OER current of a particular discontinuous sample, the K_{Edge} and K_{Area} can be solved by simultaneous equations established with the equation of CMOH-py-cont as the control reference (see the Supporting Information for the details). All the solved K_{Edge} and K_{Area} are summarized in Figure 3d as the function of discontinuity (same as the edge-to-area ratios). K_{Edge} is shown to be five orders of magnitude higher than K_{Area}, showing that the normalized activity per unit area of edge is not the same as that of the central parts of film, and the major OER contribution are indeed dominated by the edges. The values of K_{Edge} actually vary drastically with the edge-to-area ratios, as compared to K_{Area} that remains relatively constant. In addition, the K_{Edge} of CMOH-py-S is 40 times higher than CMOH-py-XL. Assuming that all of active sites on each sample are identical and yield one oxygen molecule per cycle, the edge-site atom efficiency of CMOH-py-XL is thus only 2.5% of CMOH-py-S. The key message is that the activation of edge sites has the opportunity to be further optimized by engineering edge-to-area ratios of discontinuous CMOH. The relative-constant K_{Area} would not cancel out the OER enhancement caused by edge through increasing discontinuity. Thus, overall performance prediction is that the higher edge-to-area ratios of thin films lead to the greater OER. The observation of much increased TOF and atom efficiency above due to discontinuity variation is thus understood to have originated from the edges and not from the central area of film. Thus, the higher atom efficiency on edge sites is considered to enhance OER performance much more than central area parts. In other words, massive exposure of edge sites can significantly improve OER activity.

The heterojunction edge-favored OER has been suggested due to the presence of unsatisfied, distorted coordination sites and lowered current resistance at the edges.[2,45,46] Recent studies indicate that highly OER active sites are present at the isolated edges where the core of OER-active metal complexes shows lowered coordination numbers.[45] These unsatisfied sites exhibit stronger affinity for hydroxyl ion adsorption and are able to facilitate deprotonation in OER, as indicated by theoretical calculations.[46] The distortion of metal-oxygen octahedra at the edge interfaces may additionally contribute to the OER currents.[44] In this work, the presence of unsatisfied sites may also support the lowered OER activation energy as indicated by the Raman results.

Ultrathin wedge-shape terminals, typically formed at the edges of thin film deposition, may significantly reduce the electrical resistivity,[47] so the charges are allowed to rapidly reach the triple-phase boundary regions where OER essentially occurs.[20] The SEM inspection shows the ultrathin wedge-shape and right-angle terminals of CMOH at the heterojunction edge (Figure 2m), where the spots are of low resistivity that allows rapid charge transport to the triple-phase active sites. On the other hand, the central parts (also the "nonedge area") of coating possessing a relatively high thickness build up an elevated electrical resistivity that requires stronger potentials for charges reaching the triple-phase regions. This may rationalize the relatively higher OER threshold of CMOH-py-XL observed in the Raman studies and the oxygen generation selectively around the edge in Movie S1 in the Supporting Information.

To further investigate this concept, we conducted electrochemical impedance spectroscopy (EIS) to determine the interfacial charge transport resistance at the ultrathin wedge-shape terminals. As shown in the EIS data (Figure S8, Supporting Information), the charge transfer resistance (R_{ct}) of CMOH-py-S is apparently lower than all the other samples possessing the higher film continuity, which rationalizes further that the discontinuity-dependent OER is related to the kinetics of charge transfer resistance as well.

According to all the results, one may consider that creating even higher edge-to-area ratios and quantity of edge interfaces through casting nanosize powders on electrodes for the optimal OER. By following the previous preparation of CMOH powders,[36] we were able to disperse the CMOH powders (typical diameter 80–100 nm) over gold-coated pyramid electrodes (1×1 cm^2) with identical loading mass to CMOH-py-S. The tests show the weaker OER activities and durability (i.e., 63% OER current drop within 3 h) of the powder-loaded electrodes than the thin film samples (Figure S9, Supporting Information). After the stability tests, the powder CMOH severely peeled off from the pyramid surface (see Figure S9c,d, Supporting Information). In control experiments with the higher powder loadings, we visibly observed that the black powders were detached from the electrodes, which became more significant when the electrolysis potentials were increased. These results further suggest that the weak interfacial contacts of the CMOH powder greatly compromise the long-term stability of OER. In addition to the maximized edge exposure, robust and intimate interfacial contact is also critical to realize high OER performance. Large-scale, facile engineering of thin film is therefore highly promising toward OER perfection with great commercialization values over the other systems.

Oxygen evolution from the planar substrates is visibly different from pyramidal electrodes, as shown in Movie S2 in the Supporting Information. Oxygen bubbles on the pyramidal substrates are smaller and faster and have much smaller degree of retention. As mentioned earlier, 3D features indeed improve bubble migration and departure, so the atom efficiency can be fairly compared in this study.[10] In addition, the finer sizes of oxygen bubbles reduce the energy required in OER,[48] suggesting that nonplanar 3D electrodes, such as the pyramid structures may serve as ideal, versatile platform to facilitate mass-transfer in gas evolution reactions.

3. Conclusion

We demonstrate that discontinuous thin film electrocatalysts outperform continuous ones in terms of atom efficiency and overall activities. The findings in this work show that robust thin film electrocatalytic systems can be enhanced by introducing more edges without sacrificing durability, as long as interfacial bounding is not weakened. This suggests a promising route for making high performance OER systems with long-term stability for water splitting applications. Discontinuous films can be further enhanced by deposition on 3D substrates to increase the fraction of edge sites.

Supporting Information

Supporting Information is available from the Wiley Online Library or from the author.

Acknowledgements

M.-C.S. and R.-H.J. contributed equally to this work. C.-H.C. acknowledges financial support from Ministry of Science and Technology, Taiwan under grant 107-2113-M-110-003, 105-2221-E-110-075, and 106-2221-E-110-060-MY3, part of which supports R.-H.J. and his visit to Northwestern University. The authors thank Prof. Raymand Joesten for valuable suggestions.

Conflict of Interest

The authors declare no conflict of interest.

Keywords

cobalt oxide, electrocatalysis, manganese oxide, oxygen evolution, thin films

Received: June 28, 2019
Revised: September 8, 2019
Published online: October 14, 2019

[1] R.-H. Jhang, C.-Y. Yang, M.-C. Shih, J.-Q. Ho, Y.-T. Tsai, C.-H. Chen, *J. Mater. Chem. A* **2018**, *6*, 17915.
[2] I. Roger, M. A. Shipman, M. D. Symes, *Nat. Rev. Chem.* **2017**, *1*, 0003.

[3] X. Han, C. Yu, S. Zhou, C. Zhao, H. Huang, J. Yang, Z. Liu, J. Zhao, J. Qiu, *Adv. Energy Mater.* **2017**, *7*, 1602148.
[4] X. Wang, A. Vasileff, Y. Jiao, Y. Zheng, S.-Z. Qiao, *Adv. Mater.* **2019**, *31*, 1803625.
[5] W. Liu, H. Liu, L. Dang, H. Zhang, X. Wu, B. Yang, Z. Li, X. Zhang, L. Lei, S. Jin, *Adv. Funct. Mater.* **2017**, *27*, 1603904.
[6] F. Song, L. Bai, A. Moysiadou, S. Lee, C. Hu, L. Liardet, X. Hu, *J. Am. Chem. Soc.* **2018**, *140*, 7748.
[7] B. Wang, C. Tang, H.-F. Wang, X. Chen, R. Cao, Q. Zhang, *Adv. Mater.* **2019**, *31*, 1805658.
[8] B. M. Hunter, H. B. Gray, A. M. Müller, *Chem. Rev.* **2016**, *116*, 14120.
[9] J. Shan, T. Ling, K. Davey, Y. Zheng, S.-Z. Qiao, *Adv. Mater.* **2019**, *31*, 1900510.
[10] M. B. Stevens, L. J. Enman, A. S. Batchellor, M. R. Cosby, A. E. Vise, C. D. M. Trang, S. W. Boettcher, *Chem. Mater.* **2017**, *29*, 120.
[11] L. Trotochaud, J. K. Ranney, K. N. Williams, S. W. Boettcher, *J. Am. Chem. Soc.* **2012**, *134*, 17253.
[12] M. W. Kanan, D. G. Nocera, *Science* **2008**, *321*, 1072.
[13] R. D. L. Smith, M. S. Prévot, R. D. Fagan, Z. Zhang, P. A. Sedach, M. K. J. Siu, S. Trudel, C. P. Berlinguette, *Science* **2013**, *340*, 60.
[14] C. G. Morales-Guio, L. Liardet, X. Hu, *J. Am. Chem. Soc.* **2016**, *138*, 8946.
[15] W. Zhang, Y. Wu, J. Qi, M. Chen, R. Cao, *Adv. Energy Mater.* **2017**, *7*, 1602547.
[16] J. Dong, F.-Q. Zhang, Y. Yang, Y.-B. Zhang, H. He, X. Huang, X. Fan, X.-M. Zhang, *Appl. Catal., B* **2019**, *243*, 693.
[17] M. Yao, N. Wang, W. Hu, S. Komarneni, *Appl. Catal., B* **2018**, *233*, 226.
[18] J. Huang, J. Han, R. Wang, Y. Zhang, X. Wang, X. Zhang, Z. Zhang, Y. Zhang, B. Song, S. Jin, *ACS Energy Lett.* **2018**, *3*, 1698.
[19] S. F. Hung, Y. Y. Hsu, C. J. Chang, C. S. Hsu, N. T. Suen, T. S. Chan, H. M. Chen, *Adv. Energy Mater.* **2018**, *8*, 1701686.
[20] C. Tang, H.-F. Wang, Q. Zhang, *Acc. Chem. Res.* **2018**, *51*, 881.
[21] J. Su, R. Ge, Y. Dong, F. Hao, L. Chen, *J. Mater. Chem. A* **2018**, *6*, 14025.
[22] H. Fei, J. Dong, Y. Feng, C. S. Allen, C. Wan, B. Volosskiy, M. Li, Z. Zhao, Y. Wang, H. Sun, P. An, W. Chen, Z. Guo, C. Lee, D. Chen, I. Shakir, M. Liu, T. Hu, Y. Li, A. I. Kirkland, X. Duan, Y. Huang, *Nat. Catal.* **2018**, *1*, 63.
[23] S. Su, Q. Zhou, Z. Zeng, D. Hu, X. Wang, M. Jin, X. Gao, R. Nötzel, G. Zhou, Z. Zhang, J. Liu, *ACS Appl. Mater. Interfaces* **2018**, *10*, 8026.
[24] J. Kibsgaard, Z. Chen, B. N. Reinecke, T. F. Jaramillo, *Nat. Mater.* **2012**, *11*, 963.
[25] J. Masud, A. T. Swesi, W. P. R. Liyanage, M. Nath, *ACS Appl. Mater. Interfaces* **2016**, *8*, 17292.
[26] D. R. Kauffman, X. Deng, D. C. Sorescu, T.-D. Nguyen-Phan, C. Wang, C. M. Marin, E. Stavitski, I. Waluyo, A. Hunt, *ACS Catal.* **2019**, *9*, 5375.
[27] W.-J. Lan, C.-C. Kuo, C.-H. Chen, *Chem. Commun.* **2013**, *49*, 3025.
[28] Z. Chen, L. Cai, X. Yang, C. Kronawitter, L. Guo, S. Shen, B. E. Koel, *ACS Catal.* **2018**, *8*, 1238.
[29] K. Jin, H. Seo, T. Hayashi, M. Balamurugan, D. Jeong, Y. K. Go, J. S. Hong, K. H. Cho, H. Kakizaki, N. Bonnet-Mercier, M. G. Kim, S. H. Kim, R. Nakamura, K. T. Nam, *J. Am. Chem. Soc.* **2017**, *139*, 2277.
[30] C.-C. Kuo, C.-H. Chen, *Nanoscale* **2014**, *6*, 12805.
[31] T. Tang, W.-J. Jiang, S. Niu, N. Liu, H. Luo, Y.-Y. Chen, S.-F. Jin, F. Gao, L.-J. Wan, J.-S. Hu, *J. Am. Chem. Soc.* **2017**, *139*, 8320.
[32] J. W. D. Ng, M. García-Melchor, M. Bajdich, P. Chakthranont, C. Kirk, A. Vojvodic, T. F. Jaramillo, *Nat. Energy* **2016**, *1*, 16053.
[33] C.-W. Huang, J. A. A. Valinton, Y. Hung Jr., C.-H. Chen, *Sens. Actuators, B* **2018**, *266*, 463.
[34] D. Voiry, M. Chhowalla, Y. Gogotsi, N. A. Kotov, Y. Li, R. M. Penner, R. E. Schaak, P. S. Weiss, *ACS Nano* **2018**, *12*, 9635.
[35] A. Bergmann, E. Martinez-Moreno, D. Teschner, P. Chernev, M. Gliech, J. F. de Araújo, T. Reier, H. Dau, P. Strasser, *Nat. Commun.* **2015**, *6*, 8625.
[36] C.-C. Kuo, W.-J. Lan, C.-H. Chen, *Nanoscale* **2014**, *6*, 334.
[37] D. González-Flores, I. Sánchez, I. Zaharieva, K. Klingan, J. Heidkamp, P. Chernev, P. W. Menezes, M. Driess, H. Dau, M. L. Montero, *Angew. Chem., Int. Ed.* **2015**, *54*, 2472.
[38] J. Kibsgaard, T. R. Hellstern, S.-J. Choi, B. N. Reinecke, T. F. Jaramillo, *ChemElectroChem* **2017**, *4*, 2480.
[39] S.-F. Hung, Y.-T. Chan, C.-C. Chang, M.-K. Tsai, Y.-F. Liao, N. Hiraoka, C.-S. Hsu, H. M. Chen, *J. Am. Chem. Soc.* **2018**, *140*, 17263.
[40] C.-S. Hsu, N.-T. Suen, Y.-Y. Hsu, H.-Y. Lin, C.-W. Tung, Y.-F. Liao, T.-S. Chan, H.-S. Sheu, S.-Y. Chen, H. M. Chen, *Phys. Chem. Chem. Phys.* **2017**, *19*, 8681.
[41] M. Risch, F. Ringleb, M. Kohlhoff, P. Bogdanoff, P. Chernev, I. Zaharieva, H. Dau, *Energy Environ. Sci.* **2015**, *8*, 661.
[42] I. G. McKendry, A. C. Thenuwara, S. L. Shumlas, H. Peng, Y. V. Aulin, P. R. Chinnam, E. Borguet, D. R. Strongin, M. J. Zdilla, *Inorg. Chem.* **2018**, *57*, 557.
[43] C.-H. Chen, E. C. Njagi, S.-Y. Chen, D. T. Horvath, L. Xu, A. Morey, C. Mackin, R. Joesten, S. L. Suib, *Inorg. Chem.* **2015**, *54*, 10163.
[44] Y. Heo, S. Choi, J. Bak, H.-S. Kim, H. B. Bae, S.-Y. Chung, *Adv. Energy Mater.* **2018**, *8*, 1802481.
[45] J. Fester, M. García-Melchor, A. S. Walton, M. Bajdich, Z. Li, L. Lammich, A. Vojvodic, J. V. Lauritsen, *Nat. Commun.* **2017**, *8*, 14169.
[46] M. Qin, S. Li, Y. Zhao, C.-Y. Lao, Z. Zhang, L. Liu, F. Fang, H. Wu, B. Jia, Z. Liu, W. Wang, Y. Liu, X. Qu, *Adv. Energy Mater.* **2019**, *9*, 1803060.
[47] A. Mukanova, A. Nurpeissova, S.-S. Kim, M. Myronov, Z. Bakenov, *ChemistryOpen* **2018**, *7*, 92.
[48] J. Li, Y. Zhu, W. Chen, Z. Lu, J. Xu, A. Pei, Y. Peng, X. Zheng, Z. Zhang, S. Chu, Y. Cui, *Joule* **2019**, *3*, 557.